

## Effect of Aging on the Ballistic Performance of AA-7017 Alloy

Pradipta Kumar Jena<sup>#,\*</sup>, Koppoju Suresh<sup>§</sup>, K. Sivakumar<sup>#</sup>, R.K. Mandal<sup>!</sup> and A.K. Singh<sup>#</sup>

<sup>#</sup>DRDO-Defence Metallurgical Research Laboratory, Kanchanbagh, Hyderabad - 500 058, India

<sup>§</sup>International Advanced Research Centre for Powder Metallurgy and New Materials, Hyderabad - 500 005, India

<sup>!</sup>Department of Metallurgical Engineering, IIT (BHU), Varanasi – 221 005, India

\*E-mail: pradipta.dmrl@gov.in

### ABSTRACT

This study presents the effect of aging on microstructure, texture, mechanical and ballistic properties of AA-7017 aluminium alloy. AA-7017 alloy is subjected to three different aging namely under-aging, peak-aging and over-aging. Significant difference is observed in the mechanical properties after aging. The alloy exhibits maximum strength and hardness in the peak-aged condition. From texture measurements, it is noticed that the overall intensity of orientation distribution function increases from under-aged to peak-aged condition. The AA-7017 aged plates are impacted with 7.62 mm steel core projectiles at 820±10 m/s to evaluate the ballistic performance. It is noticed that AA-7017 alloy displays best ballistic resistance in peak-aged condition. Distorted material flow lines and adiabatic shear band induced cracking is detected in post ballistic microstructure. The ballistic performance of AA-7017 alloy is correlated with the variations in the microstructure and mechanical properties with aging.

**Keywords:** 7XXX Al alloy; Aging; Texture; Mechanical property; Ballistic property

### 1. INTRODUCTION

Armour is a means of protection used to prevent damage to individuals or vehicles from projectiles during combat. At present, steels are the most commonly used armour material. Several investigators have evaluated the effect of different parameters of steel on its ballistic performance. Further improvement in ballistic impact resistance can be achieved by exploring both the new materials as well as novel thermo-mechanical processing techniques.

Ballistic performance depends on numerous material parameters namely hardness, strength, impact energy, texture and extent of deformation. A number of previous studies have attempted to correlate the ballistic performance with mechanical properties of materials. Majority of them have illustrated about the increase in ballistic performance with strength and hardness of the target material. Some other studies have associated the ballistic performance with ductility and impact toughness of materials.

Aluminium alloys have shown promise for ballistic application due to its high strength to weight ratio<sup>1-2</sup>. Age-hardenable aluminium alloy AA-7017 is noteworthy owing to its attractive properties such as high strength, good ductility and energy absorption capability. This work illustrates the ballistic performance of AA-7017 alloy in different aging conditions.

### 2. EXPERIMENTAL PROCEDURE

The chemical composition of AA-7017 alloy was determined using inductively coupled plasma optical emission

spectrometer (ICP OES, Ultima Expert) and is shown in Table 1. The material was purchased from Alcan International (U.K.) as 70 mm thick rolled plates. The as received plates were further hot rolled to 40 mm thick plates. The plates were subjected to solutionization at 455°C for 1.5 hours followed by water quenching to room temperature. The plates were artificially aged to under-aged (UA), peak-aged (PA) and over-aged (OA) condition. The parameters used for ageing are given in Table 2.

**Table 1. Analysed chemical composition of AA-7017 plate**

Composition (Wt %)	5.2 Zn, 2.3 Mg, 0.35 Si, 0.35 Cr, 0.45 Fe, 0.2 Mn, 0.1 Zr, balance Al
--------------------	---

**Table 2. Heat treatment schedule for different aging conditions**

Material	Aging condition	Heat treatment parameters	Cooling
AA-7017	Under-aged	1h at 130°C	Air Cooling
	Peak-aged	8h at 130°C	Air Cooling
	Over-aged	24h at 130°C	Air Cooling

Differential scanning calorimetry (DSC) studies were carried out to understand the sequence of precipitation of the AA-7017 alloy. DSC experiments were conducted at 20°C/min heating rate using a NET2SCH instrument (204FI Phoenix model). X-ray diffraction (XRD) experiments of the aged AA-7017 plates were performed in a Philips 3020 diffractometer. In order to measure texture, 25×15 mm<sup>2</sup> samples were prepared from the aged plates. The texture measurement of the aged

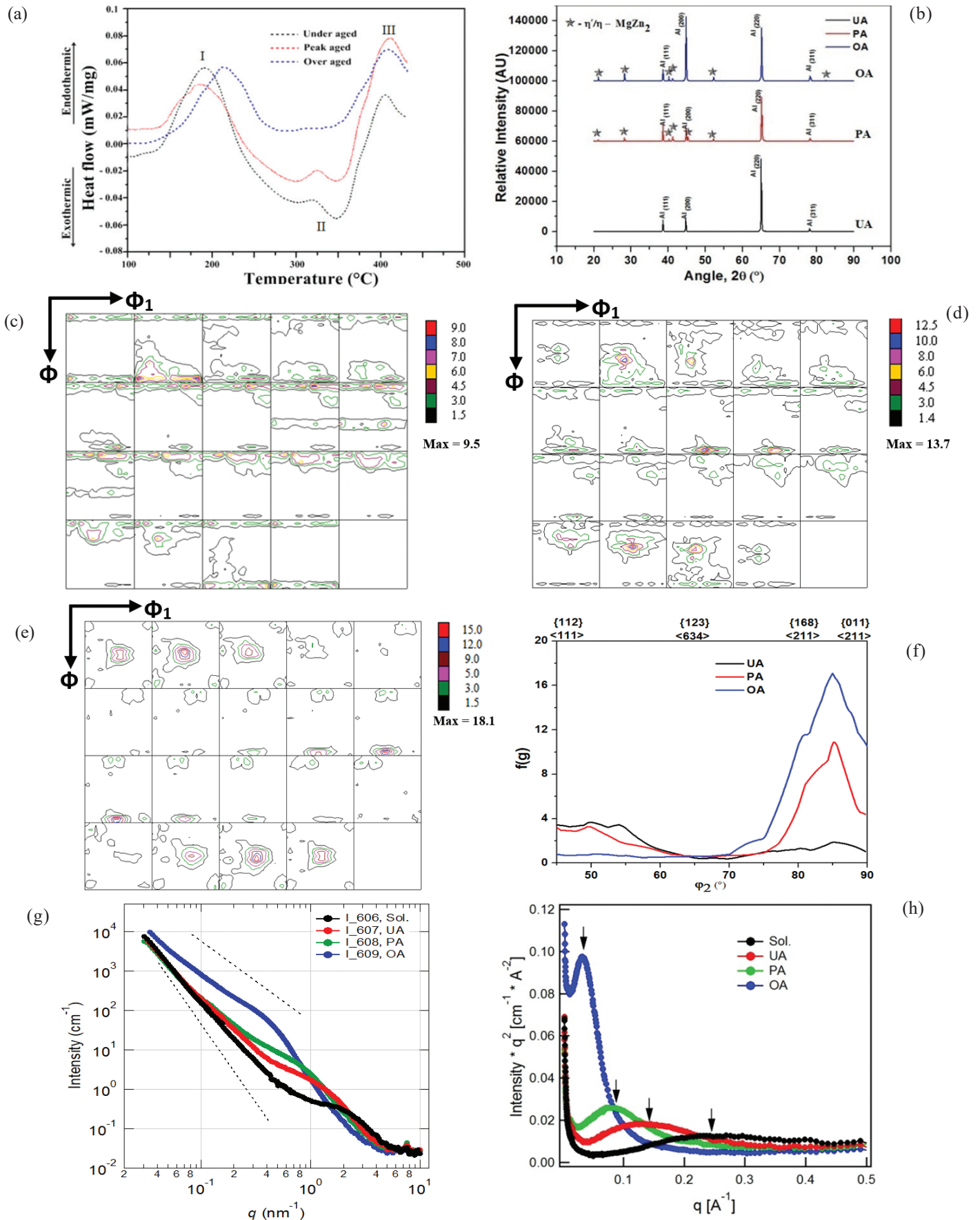


Figure 1. (a) DSC thermograms and (b) X-ray diffractograms of AA 7017 in UA, PA, OA condition (c) ODF of UA (d) ODF of PA and (e) ODF of OA sample (f)  $\beta$  fibres of UA, PA and OA samples (g) intensity vs. scattering wave vector ( $q$ ) plots and (h) Kratky plots in solution treated and aged condition.

samples was carried out by Schultz back technique using an inel G3000 texture goniometer<sup>3</sup>. X-ray small angle scattering experiments (make: Anton Paar, Austria) were executed to assess the size distribution of precipitates in the aged samples. The sample thickness for SAXS analysis was 80 microns. Glassy carbon was used as secondary intensity calibration standard. For q position, i.e., x-axis calibration silver behenate is used.

Tensile samples were prepared from the aged plates according to ASTM E8-93 standard and tested at  $8.3 \times 10^{-4} \text{ s}^{-1}$  strain rate. Charpy samples were machined from the aged

**Table 3. Size (D), Volume fraction ( $V_v$ ) and Number density ( $d_N$ ) of  $\text{MgZn}_2$  precipitates at different aging conditions**

Aging condition	$\langle D \rangle$ (nm)	$V_v^*$ (%)	$d_N^*$ ( $\times 10^{17} \text{ cm}^{-3}$ )
Solution treated	1.5	2.7	67
UA	2.7	6.3	15
PA	3.8	6.9	3.9
OA	9.7	6.7	0.38

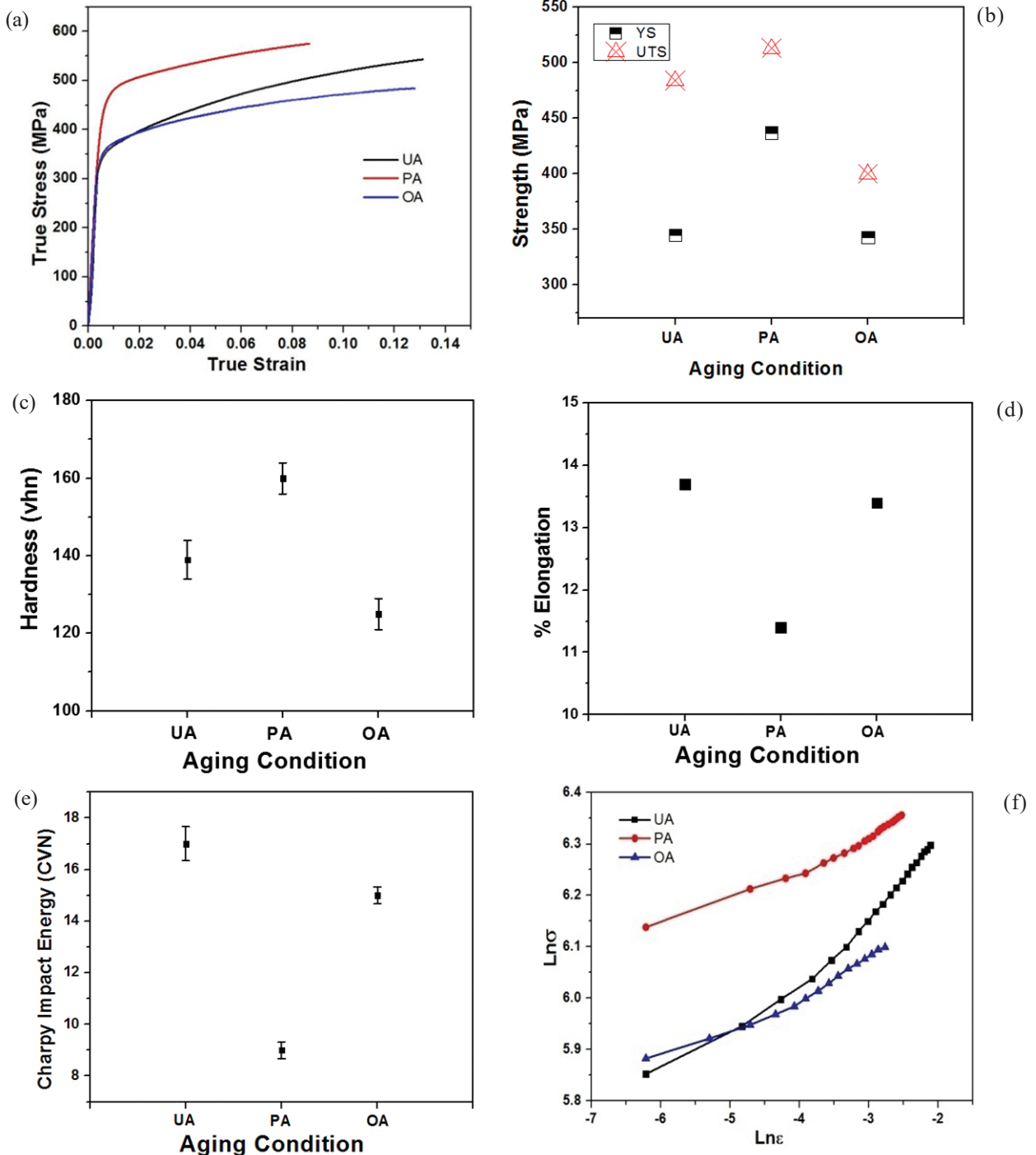


**Figure 2. (a) True stress-true strain curves; Variation of (b) Strength (c) Hardness (d) % Elongation (e) Charpy impact toughness with aging and (f) log (true stress) vs. log (true plastic strain) curves of AA-7017 alloy at different aging conditions.**

plates as per ASTM E23-02a standard. Hardness values of the aged plates were measured on a Vicker's hardness tester following ASTM E140-02 standard. Fracture surface of the Charpy samples were investigated under a FEI scanning electron microscope to understand the topographical features. 200×100×40 mm<sup>3</sup> samples were machined to evaluate the ballistic property of the aged plates. The aged AA-7017 samples were impacted with 7.62 mm steel core projectiles at 820±10 m/s. The ballistic testing procedure is described in a detailed manner elsewhere<sup>4</sup>.

### 3. RESULTS

The DSC thermograms for differently aged AA-7017 samples are given in Fig 1(a). UA and PA samples display three distinct regimes with temperature: an endothermic reaction region (regime I), an exothermic reaction doublet (regime II) and an endothermic reaction (regime III). In contrast, the exothermic region is absent in OA specimen. In addition, the temperature range of the region I is also shifted to higher temperature.

Figure 1(b) exhibits X-ray diffractograms of AA-7017 alloy at different aging conditions. From the XRD pattern a face-centered-cubic (fcc) matrix phase with lattice constant ~4.05 Å is obtained. A few small peaks corresponding to the η (MgZn<sub>2</sub>) and η' (MgZn<sub>2</sub>) phases are observed in the XRD patterns of the PA and OA plates. The texture of the aged plates in terms of orientation distribution functions (ODF) are shown in Fig. 1(c-e).

There is a variation observed in the overall texture intensity of the aged plates. The maximum overall ODF intensities in UA, PA and OA plates are 9.5, 13.7 and 18.1, respectively. The major texture components for UA, PA and OA plates are {103}⟨331⟩[f(g)=3.4], {0,1,12}⟨7,12,1⟩[f(g)=4.1], {0,1,12}⟨2,12,1⟩[f(g)=4.2], {203}⟨302⟩[f(g)=6.1], {001}⟨100⟩[f(g)=1.7], {112}⟨132⟩[f(g)=6.0], {113}⟨031⟩[f(g)=7.7], {111}⟨011⟩[f(g)=6.5], {114}⟨110⟩[f(g)=5.0], {114}⟨041⟩[f(g)=6.2], {111}⟨110⟩[f(g)=6.6], {103}⟨331⟩[f(g)=2.1], {0,1,12}⟨10,12,1⟩[f(g)=2.3], {011}⟨100⟩[f(g)=3.9], {104}⟨401⟩[f(g)=1.8], {1,1,15}⟨2,13,1⟩[f(g)=3.0], {1,1,15}⟨6,9,1⟩[f(g)=3.2], {225}⟨232⟩[f(g)=3.2], {113}⟨110⟩[f(g)=3.8], {441}⟨104⟩[f(g)=4.8] and {001}⟨655⟩[f(g)=10.4], {551}⟨110⟩[f(g)=15.6].

The texture component intensities [f(g)] are presented as "times random". The β fibers of the UA, OA and PA plates are exhibited in Fig. 1(f). The β fibre is very weak in UA plate, while inhomogeneous with high intensity between {168}⟨211⟩ and {011}⟨211⟩ locations in PA and OA plates.

The intensity vs. scattering wave vector (q) plots of AA-7017 alloy in different aged conditions is displayed in Fig. 1(g). The corresponding Kratky plots are displayed in Fig. 1(h). This clearly reflects strong scattering in solution treated sample indicating the presence of fine precipitates which corresponds to GP zones. The aged (UA, PA and OA) samples reflect the presence of MgZn<sub>2</sub> precipitates. The size, number density and volume fractions of the MgZn<sub>2</sub> precipitates are obtained using standard SAXS calculation using IRENA size distribution macros and are given in Table 3. The contrast factor was estimated by considering only MgZn<sub>2</sub> precipitates.

**Table 4. Strain hardening exponents of AA-7017 alloy at different aging conditions**

Heat treatment condition	n <sub>1</sub>	-n <sub>2</sub>
Under-aged	0.156	106
Peak-aged	0.082	131
Over-aged	0.088	195.4

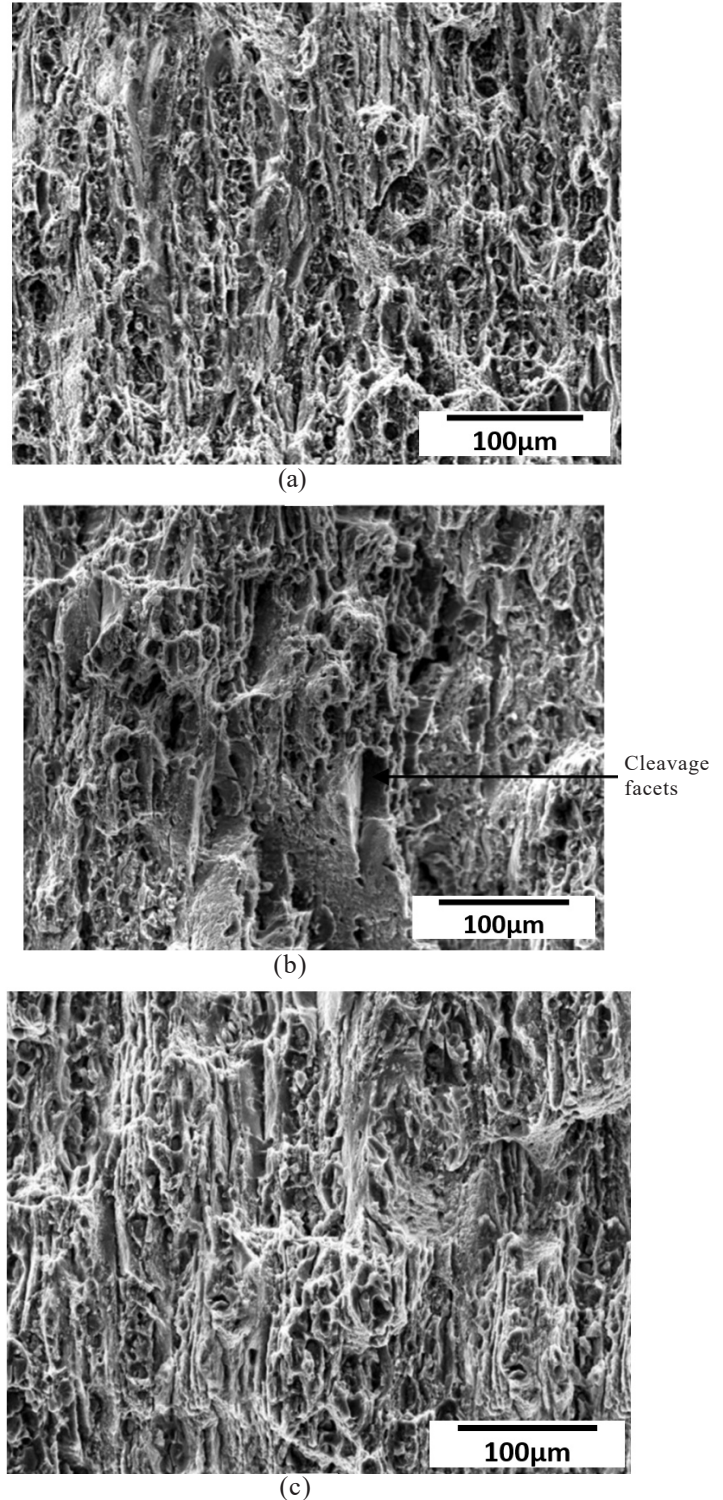


**Figure 3. Fractographs of impact fracture surface of differently aged plates (a) UA (b) PA and (c) OA.**

True stress-strain curves of AA-7017 alloy in different aged condition are given in Fig. 2(a). The mechanical properties are illustrated in Fig. 2(b-e). The alloy in PA condition exhibits maximum hardness, yield ( $\sigma_{YS}$ ) and tensile strength ( $\sigma_{UTS}$ ), whereas UA condition displays maximum ductility. In all the aging conditions two slopes are observed in the strain hardening curves (Fig. 2f). Ludwигson's relation (Eqn. 1) is employed to measure the strain hardening exponent ( $n$ ) at different strain regimes<sup>5</sup>.

$$\sigma = K_1 \varepsilon^{n_1} + \exp(K_2 + n_2 \varepsilon) \quad (1)$$

Where  $\sigma$  is true plastic stress,  $\varepsilon$  is true plastic strain,  $K_1$  and  $n_1$  are as same as  $K$  and  $n$  in the Ludwik relation.  $K_2$  and  $n_2$  are the constituents of a term which describes the positive departure of flow curve from the Ludwik relation at low strains. Table 4 gives the ' $n_1$ ' and ' $n_2$ ' values of the aged plates. It can be observed that in the high strain regime, the strain hardening exponent decreases from UA to PA condition and shows a

marginally increase in OA plate. In the low strain regime, the strain hardening exponent decreases continuously from UA to OA condition.

The Charpy impact test results of UA, PA and OA samples are shown in Fig. 2(e). UA and PA plates display the maximum (17J) and minimum (9J) values of impact energy, respectively. Fig. 3 displays the changes in fractographic features with aging. The fracture surface of UA and PA plates mainly show ductile dimples. In PA samples, cleavage facets are also observed along with dimples in the fracture surface.

The aged AA-7017 plates after ballistic testing are shown in Fig. 4(a). It can be seen that the projectiles penetrated through the UA plates and the tip is seen protruding out at the back side of the plates. There is a complete perforation observed in OA plates. In contrast, the PA plates are able to stop the projectiles successfully. Petalling is observed in UA and PA plates. On the other hand, spalling is seen in the PA plates. The microstructure close to the impact craters is studied



Figure 4. (a) Aged plates after ballistic impact.

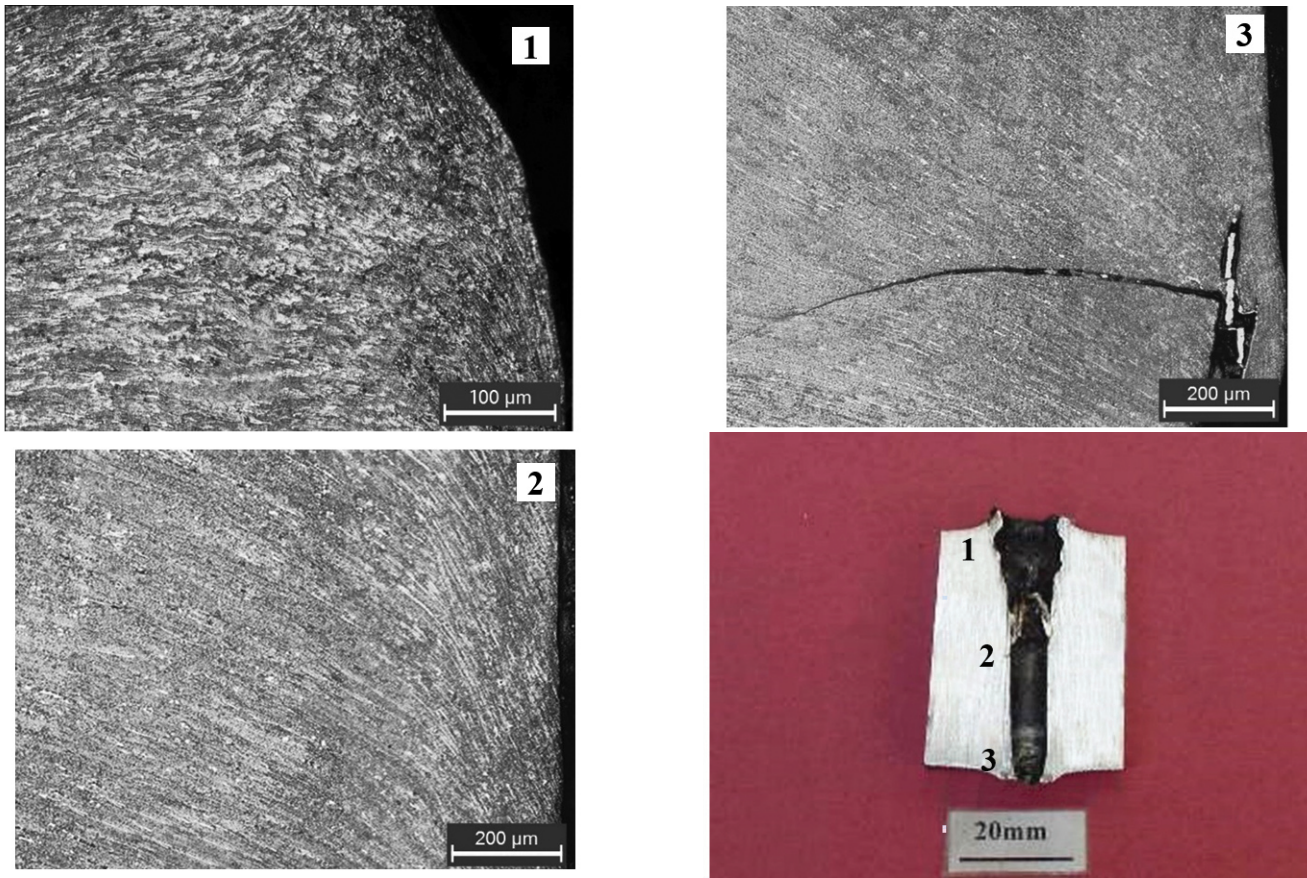


Figure 4. (b) Post ballistic microstructure of UA plates after ballistic impact.

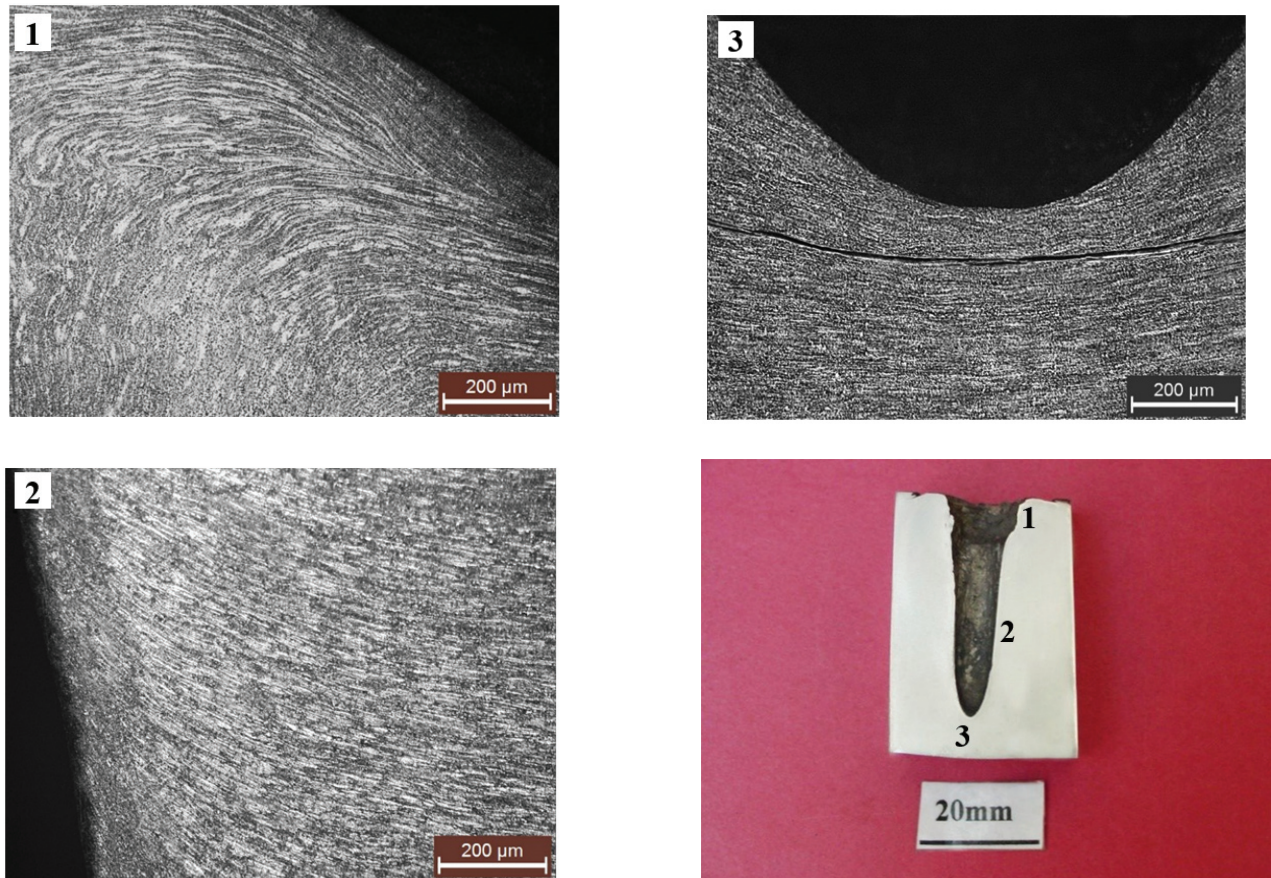


Figure 4. (c) Post ballistic microstructure of PA plates after ballistic impact.

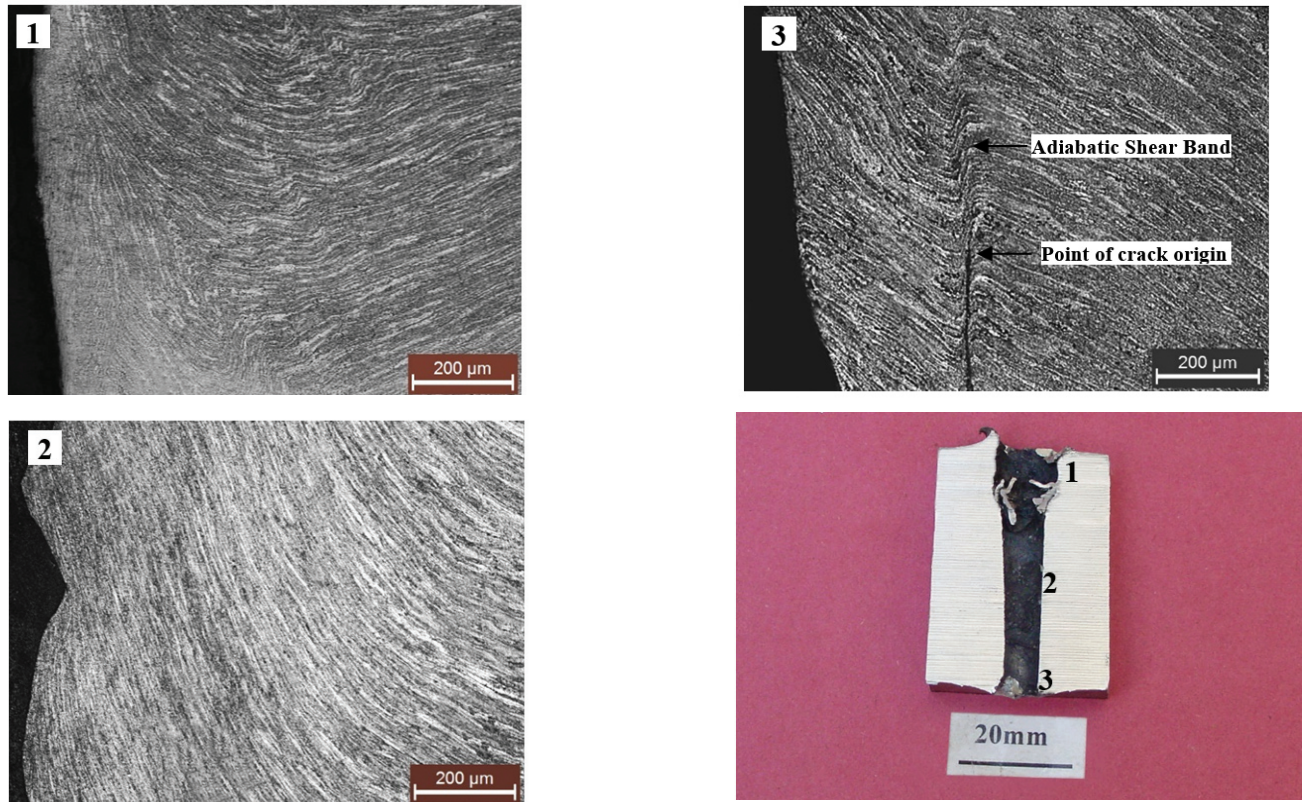


Figure 4. (d) Post ballistic microstructure of OA plates after ballistic impact.

to understand the material behavior during ballistic impact (Fig. 4(b-d)). Similar microstructural features are observed in all the aged plates. Distorted material flow lines with adiabatic shear bands (ASBs) are seen at the projectile entry region. Beyond that the flow lines become smooth and bent along the penetration direction. Small cracks are noticed emanating from the crater wall in all the plates. The microstructure of the crater region also displays ASBs leading to the cracks. The UA plate exhibits maximum number of ASBs.

#### 4. DISCUSSION

Al-Zn-Mg alloys undergo decomposition during aging<sup>6</sup>: Super saturation solid solution (SSSS)  $\rightarrow$  Guinier Preston (GP) zones  $\rightarrow$  Semi-coherent  $\eta'$  ( $\text{MgZn}_2$ )  $\rightarrow$  Incoherent  $\eta$  ( $\text{MgZn}_2$ ). The strong scattering observed in log – log plot of intensity vs.  $q$  (scattering wave vector) in solution treated condition corresponds to quenched GP zones. Precipitation sequence can furthermore be realised from the different regions of the DSC thermograms (Fig 1(a)). It is to be noted that in precipitation hardenable aluminum alloys, precipitation and dissolution processes are exothermic and endothermic, respectively<sup>7</sup>. The first endothermic region (region I) represents the dissolution of GP zones. The doublet observed in the exothermic reaction in region 2 is attributed to the separate sequential reactions involving  $\eta'$  ( $\text{MgZn}_2$ ) formation, dissolution of  $\eta'$  ( $\text{MgZn}_2$ ) and subsequently formation of  $\eta$  ( $\text{MgZn}_2$ )<sup>8</sup>. The higher temperature endotherm (region 3) illustrates the dissolution of  $\eta$  ( $\text{MgZn}_2$ ) precipitates. Since the OA material contains  $\eta'$  ( $\text{MgZn}_2$ ) and  $\eta$  ( $\text{MgZn}_2$ ) precipitates, the intermediate exothermic reaction (region 2) is absent in its DSC thermograms.

The shifting of peak of the endothermic reaction region I to higher temperature for OA material has been related to size of the  $\eta$  ( $\text{MgZn}_2$ ) precipitates. The coarse  $\eta$  ( $\text{MgZn}_2$ ) precipitates in OA condition reduces the solubility and hence increases the temperature of dissolution. In a previous study it has been reported that the size of the  $\eta$  ( $\text{MgZn}_2$ ) precipitates increases from 35  $\mu\text{m}$  in PA to 90  $\mu\text{m}$  in OA in AA-7017 alloy<sup>9</sup>. The present results based on SAXS exhibit that the average diameter and volume fraction of  $\text{MgZn}_2$  precipitates increase significantly from UA to PA to OA conditions. The precipitation sequence and the peak temperatures of the differently aged specimens are in agreement with previously reported other 7 $\times\times\times$  series aluminium alloys<sup>10</sup>. Prominent peaks of  $\eta'$  and  $\eta$  precipitates are also observed in XRD diffraction pattern of PA and OA plates (Fig. 1b). This reinforces the sequence of precipitation during aging as mentioned above.

From the texture measurements, the overall intensity of ODF increase from UA to OA plates (Fig. 1(c-e)). UA plates show recrystallisation texture components observed in fcc materials. A continuous fibre is also observed between  $\varphi=0$  to  $90^\circ$  in  $\varphi_2 = 0^\circ$  section. It appears that these components are moving towards typical cube texture during aging. The aging of hot rolled material at relatively low temperature align the existing components and move them towards either recovery or the stable end orientation in particular in case of recrystallization. However, the aging time and temperature of UA material is not sufficient for complete recrystallisation. This is reflected in the low intensity of the  $\beta$  fibre which is nearly homogeneous. The PA material, on the other hand, displays high intensity between  $\{168\}\langle 211\rangle$  and  $\{011\}\langle 211\rangle$  orientations in  $\beta$  fibre and several

other components with reasonable intensities. The continuous fibre between  $\varphi=0$  to  $90^\circ$  in  $\varphi_2 = 0^\circ$  is broken. The texture is quite sharp in OA material. The main component is also close to typical Bs component. This corresponds to high intensity between  $\{168\}\langle 211\rangle$  and  $\{011\}\langle 211\rangle$  locations in  $\beta$  fibre. The cube component further weakens in OA material.

Strength and hardness values display an increase and decrease from UA to PA and PA to OA plates, respectively (Fig. 2b-c). Previous studies have also reported similar change in strength and hardness with aging time<sup>11-12</sup>. The deviation in strength and hardness can be explained from the changes in morphology of the precipitate phases. The maximum strength and hardness in PA condition is due to the formation of large

numbers of fine  $\eta'$  ( $\text{MgZn}_2$ ) precipitates within the matrix. The decrease in strength and hardness value for the OA condition can be attributed to the transformation of metastable  $\eta'$  precipitates ( $\text{MgZn}_2$ ) phase to stable  $\eta$  ( $\text{MgZn}_2$ ) phase and the growth of the  $\eta'$  ( $\text{MgZn}_2$ ) precipitates. In UA condition, cutting through of dislocations is the dominating mechanism as the size of the  $\text{MgZn}_2$  precipitates are small. In PA condition, maximum strength is obtained at a critical radius of the strengthening  $\text{MgZn}_2$  precipitates, as higher stress is required for dislocations to cut through them<sup>13</sup>. With further increase in diameter of the  $\text{MgZn}_2$  precipitates, looping of dislocations become the dominating mechanism in OA condition. As lower stress is required for dislocations to loop around the bigger  $\eta'$

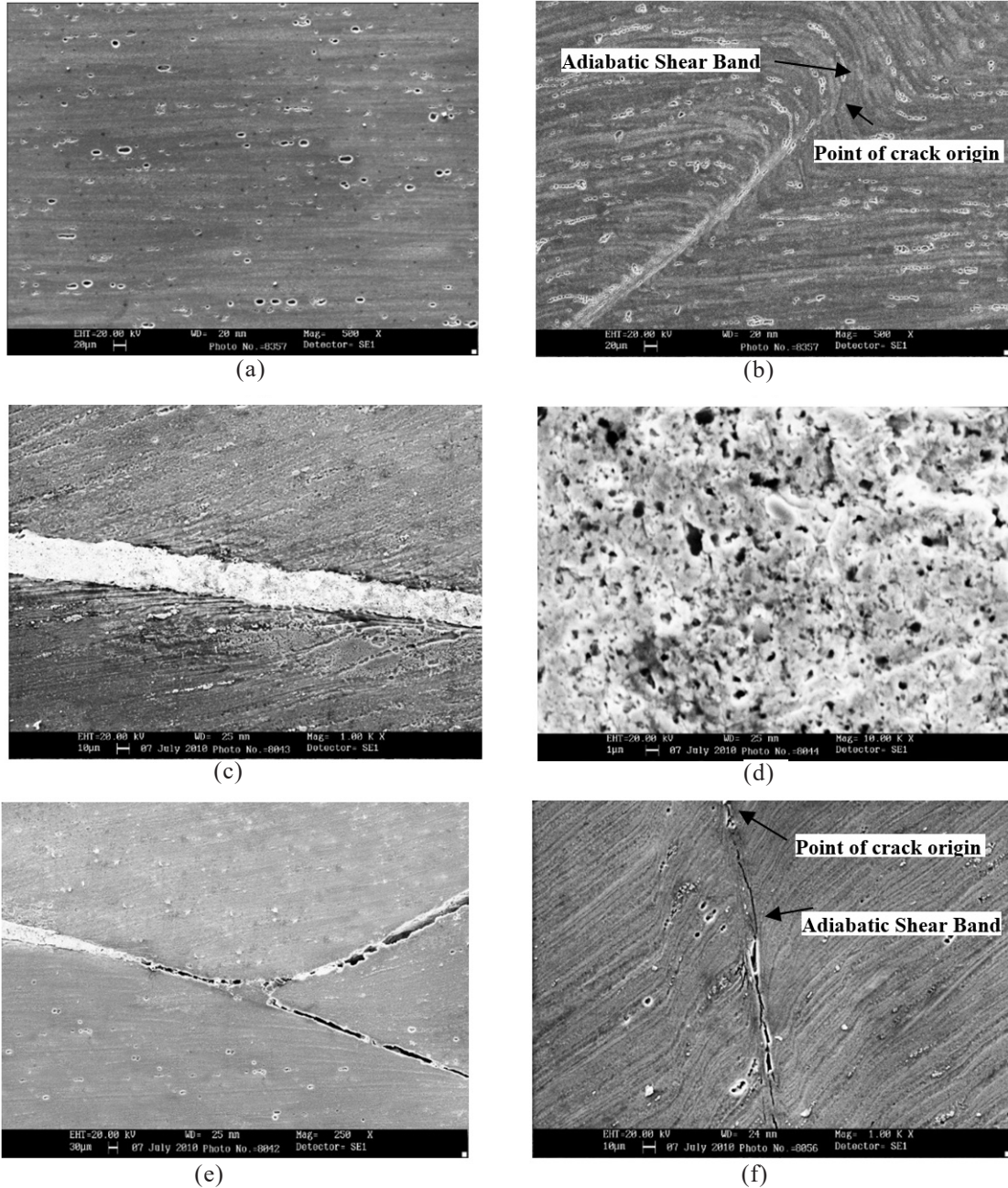


Figure 5. SEM images: (a) Intermetallic particles aligned in the rolling direction, (b) Intermetallic particles aligned in the shear flow direction in deformed ASBs, (c) Absence of bigger intermetallic particles in transformed ASBs, (d) Close view of the centre region of transformed ASBs, (e) Bifurcation of ASBs in PA and OA specimens, and (f) Cracks originating from deformed ASBs.

(MgZn<sub>2</sub>) precipitates, it subsequently leads to a decrease in the strength of the material in OA condition. This also explains the decrease and increase of ductility from UA to PA and PA to OA plates, respectively (Fig. 2d).

The two - slope behaviour of the plastic stress-strain curves indicates two different deformation mechanisms in the aged AA-7017 samples (Fig. 2f). Planar flow of dislocations is the dominating mechanism in low strain region, whereas cross slip is the controlling mechanism in high strain regimes<sup>5</sup>. Two - slope behaviour in flow curves has also been reported in other fcc materials<sup>14</sup>. The drop in 'n<sub>1</sub>' value from UA to PA materials can be ascribed to the cutting of the coherent precipitates by dislocations<sup>15</sup>. As the precipitates slacken coherency, the value of 'n<sub>1</sub>' again increases marginally from PA to OA materials. The gradual drop in 'n<sub>2</sub>' values from UA to PA and PA to OA materials can be assigned to the subsequent ease of cross slip with progress of ageing process. Strain hardening exponent 'n' offers a good indication about the propensity of deformation in terms of spread of dissipation energy in the material at high strain rates. Higher 'n' value implies that the deformation can be spread over a bigger area without getting localised. In turn, the material deforms in a homogeneous manner and can absorb more impact energy. The dimple morphology in the fracture surfaces of UA and OA plates indicate a ductile mode of failure consisting of void nucleation, growth and coalescence (Fig. 3). This gives maximum impact energy to the UA plates.

In PA material, the cleavage facets reduce the energy necessitate to fracture and hence decreases the Charpy impact energy. The cleavage facets are formed due to a combination of low ductility and precipitate free zones along grain boundaries in PA condition.

There are two material parameters, namely, (i) hardness and (ii) toughness which are important for optimizing the ballistic performance. Target plate hardness resists the penetration and facilitates the fracture of the projectile. Higher toughness assists in absorbing the impact energy in a uniform manner. Therefore, toughness also supplements to the ballistic

resistance of the material. The PA plate exhibits higher ballistic performance owing to superior strength and hardness values. UA plates display highest ductility and Charpy impact values but they show inferior ballistic property in comparison to PA plates. Thus, it appears that the material hardness is a key factor in comparison to other mechanical properties to tailor the ballistic performance. This is in agreement with previous investigations<sup>16</sup>.

The texture of the aged plates has also played a vital role in defining the ballistic performance. It is well understood that the high intensity texture provides limited orientation of grains. It has been reported that a strong Bs texture results in the activation of only a limited number of slip systems<sup>17</sup>. It implies that the limited crystal orientations are available for the dissipation of the projectile kinetic energy with increase in intensity of texture. Thus, the presence of texture introduces a gradual non-uniform dissipation of energy during ballistic impact from UA to OA plates. The non-uniform dissipation of impacted energy impairs the ballistic performance of materials<sup>18</sup>. The lowest ballistic resistance of OA plate can be attributed to the near Bs texture as main component. In PA plates, few weak components along with Cu and Bs type main texture components are observed. These texture components provide several orientations for the dissipation of impact energy. The spread of impact energy along several orientations thus improves ballistic performance.

Heterogeneous deformation leading to the formation of ASBs is noticed in the microstructures of the impacted AA-7017 alloy plates (Fig. 4(b-d)). ASBs are formed due to the intense localized heating during ballistic impact. Both deformed and transformed ASBs are witnessed in the post ballistic microstructure. From the SEM investigation, the intermetallic particles are seen aligned along the rolling direction of the plate (Fig 5(a)). In contrast, the intermetallic particles are co-ordinated in shear flow direction in deformed ASBs (Fig 5(b)). It suggests that the significant amount of thermal softening is taking place due to adiabatic heating during deformation.

**Table 5. Parameters taken for BPI calculation at different aging conditions of AA-7017 alloy**

Aging condition	Density ( $\rho$ ) gm/cc	Elastic modulus (E) GPa	Yield strength ( $\sigma_y$ )	Tensile strength ( $\sigma_u$ )	Fractional elongation ( $\epsilon_r$ )	Poisson's ratio ( $\gamma$ )	BPI
UA	2.78	72.14	343	483	0.13	0.31	1.96
PA	2.78	77.1	437	512	0.11	0.32	1.99
OA	2.78	75.2	343	410	0.08	0.308	1.84

**Table 6. Parameters considered for BPI calculation of different materials**

Material	Density ( $\rho$ ) gm/cc	Elastic modulus (E) GPa	Yield strength ( $\sigma_y$ )	Tensile strength ( $\sigma_u$ )	Fractional elongation ( $\epsilon_r$ )	Poisson's ratio ( $\gamma$ )
Mild steel	7.8	203	325	691	0.35	0.33
RHA	7.8	200	875	975	0.2	0.30
Ti-6Al-4V	4.5	114	1059	1149	0.105	0.34
AA 2024	2.78	72.4	310	457	0.16	0.33
AA 6061	2.7	68.9	250	294	0.11	0.33
AA 7075	2.81	71.7	503	572	0.11	0.33

There is an apparent difference in the microstructures of transformed ASBs from the deformed ASBs and the bulk material (Fig. 5(c)). It is observed that transformed ASBs are without the bigger elliptical shaped intermetallic particles. The intermetallic particles appear to have dissolved inside the transformed bands during ballistic impact. The microstructure of the transformed ASBs could not be resolved under the SEM except the presence of fine round particles Fig. 5(d). It indicates the dissolution of the intermetallic particles along with the remaining un-dissolved particles.

It is interesting to notice the bifurcation of ASBs in the impacted microstructure of PA and OA specimens (Fig. 5e). The presence of shearable precipitates promotes co-planar slip in PA and OA condition. In such conditions, limited slip systems are active. This may restrict the shear band formation to one or two slip planes and create bifurcation in the slip bands followed by cracking. In UA condition, the slip is more homogeneous, and the shear band may follow the direction of the maximum shear stress and not influenced by the orientation of the slip planes. This may be the reason for no bifurcation. The bifurcation of ASBs has also been observed in AA 7075 alloy<sup>19</sup>. The cracks are seen originating from the ASBs (Fig. 5(b,f)). The initiation of cracks can be explained from the difference in visco-plasticity between the soft ASB region and the rigid adjacent material. The tensile stresses caused due to the difference between two regions lead to the initiation of cracks inside ASBs.

In an attempt to correlate the ballistic behaviour of materials in a quantitative manner, Srivathsa, *et al.* have developed an empirical model that defines a parameter called “ballistic performance index (BPI)”<sup>20</sup>. The BPI is useful in comparing the relative ballistic performance of materials with reasonably good accuracy. In the present study, the BPI values of UA, PA and OA plates are calculated using the data shown in Table 5. It is observed that the BPI value of the PA plates display the highest followed by UA and OA plates (Table 5).

To compare ballistic performance of AA-7017 with other materials used for ballistic applications, the BPI of a wide range of metallic materials e.g. mild steel, rolled homogeneous

armour (RHA) steel, AA-6061, AA-2024, AA-7075 and Ti-6Al-4V have been calculated. The experimental data required for the calculation of BPI of these materials have been taken from the previous studies<sup>20-23</sup> and are given in Table 6. For aluminium alloys, the peak-aged condition (T6) is considered for the calculations as it gives the maximum hardness. In all the cases, projectile striking velocity is considered as 820 m/s. From comparative BPI values presented in Fig. 6, it is observed that ballistic performance of AA-7017 alloy is superior to steels and other aluminium alloys. This makes AA-7017 alloy a very attractive and promising material for ballistic applications.

## 5. CONCLUSIONS

- Ballistic performance of aged AA-7017 plates against 7.62 mm steel projectiles is consistent with their hardness and strength values
- The ballistic behaviour of AA-7017 aged plates follow corresponding BPI values.

## REFERENCES

1. Forrestal, M.J.; Rosenberg, Z.; Luk, V.K. & Bless, S.J. Perforations of aluminum plates with conical-nosed projectiles. *J. Appl. Mech.*, 1987, **54**(1), 230-32. doi: 10.1115/1.3172966
2. Demir, T.; Ubeyli, M. & Yildirim, R.O. Investigation on the ballistic impact behavior of various alloys against 7.62 mm armor piercing projectile. *Mater. Des.*, 2008, **29**, 2009-16. doi: 10.1016/j.matdes.2008.04.010
3. Schultz, L.G. A direct method of determining preferred orientation of a flat reflection sample using Geiger counter X-ray spectrometer. *J. Appl. Phys.*, 1949, **20**, 1030-33. doi: 10.1063/1.1698268
4. Jena, P.K.; Jagtap, N.; Siva Kumar, K. & Bhat, T.B. Some experimental studies on angle effect in penetration. *Int. J. Impact Eng.*, 2010, **37**, 489-501. doi: 10.1016/j.ijimpeng.2009.11.009
5. Ludwigson, D.C. Modified stress-strain relation for FCC metals and alloys. *Metall. Trans.*, 1971, **2**, 2825-28. doi: org/10.1007/BF02813258
6. Werenkiold, J.C.; Deschamps, A. & Brechet, Y. Characterization and modeling of precipitation kinetics in an Al-Zn-Mg Alloy. *Mater. Sci. Eng. A.*, 2000, **293**(1-2), 267-274. doi: 10.1016/S0921-5093(00)01247-8
7. Mukhopadhyay, A.K.; Tite, C.N.J.; Flower, H.M.; Gregson, P.J. & Sale, F. Thermal analysis of the precipitation reactions in Al-Li-Cu-Mg-Zr alloys. *J. de Physique.*, 1987, **48**, 439-46. doi: 10.1051/jphyscol:1987350
8. Delasi, R. & Adler, P.N. Calorimetric Studies of 7000 Series Aluminum Alloys: I. Matrix Precipitate Characterization of 7075. *Metal. Trans. A*, 1977, **8A**, 1177-83. doi:10.1007/BF02667403
9. Rout, P.K. & Ghosh, K.S. Aging and electrochemical behaviour of 7017 Al-Zn-Mg Alloy of various temps. *Mater. Sci. Forum.*, 2012, **710**, 665-670. doi:10.4028/www.scientific.net/MSF.710.665

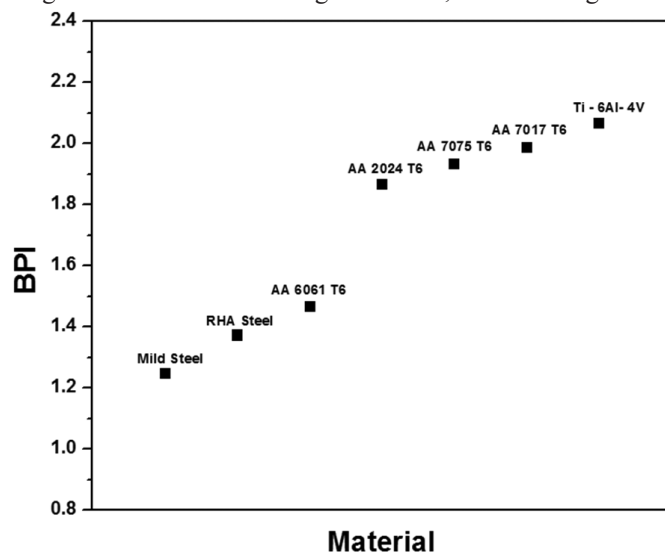


Figure 6. Ballistic Performance Index (BPI) of different materials.

10. Park, J.K. & Ardell, A.J. Co-relation between microstructure and calorimetric behavior of Aluminum alloy 7075 and Al-Zn-Mg alloys in various tempers. *Mater. Sci Eng A.*, 1989, **114**, 197-203.  
doi: 10.1016/0921-5093(89)90859-9
11. Rout, P.K.; Ghosh, M.M. & Ghosh, K.S. Influence of aging treatments on alterations of microstructural features and stress corrosion cracking behavior of an Al-Zn-Mg alloy. *J. Mater. Eng. Perform.*, 2015, **24**, 2792-2805.  
doi:10.1007/s11665-015-1559-1
12. Dumont, D.; Deschamps, A. & Brechet Y. On the relationship between microstructure; strength and toughness in AA 7050 Al alloys. *Mater. Sci. Eng. A*, 2003, **356**, 326-36.  
doi:10.1016/S0921-5093(03)00145-X
13. Gu, Gang.; Ye, Ling-ying.; Jiang, Hai-chun.; Sun, Da-xiang.; Zhang, Pan. & Zhang, Xin-ming. Effects of T916 thermo-mechanical process on microstructure, mechanical and ballistic resistance of 2519A aluminium alloy. *Trans. Nonferrous Met. Soc. China*, 2014, **24**, 2295–2300.  
doi:10.1016/S1003-6326(14)63347-1
14. Mehta, K.K.; Mukhopadhyay, P.; Mandal, R.K. & Singh, A.K. Mechanical properties anisotropy of cold rolled and solution annealed Ni–20Cr–8Fe alloy. *Mater. Sci. Eng. A*, 2014, **613**, 71–81.  
doi:10.1016/j.msea.2014.06.067
15. Sharma, V.M.J.; Sree Kumar, K.; Nageswara Rao, B. & Pathak, S.D. Studies on the work-hardening behavior of AA2219 under different aging treatments. *Metal. Trans. A.*, 2009; **40A**, 3186-95.  
doi:10.1007/s11661-009-0062-4
16. Borvik, T.; Dey, S. & Clausen, A.H. Perforation resistance of five different high strength steel plates subjected to small-arms projectiles. *Int. J. Impact Eng.* 2009, **36**, 948–64.  
doi:10.1016/j.ijimpeng.2008.12.003
17. Chang, S.C.; Jiang, Q.D.; Hu J.R. & Chen F.R., The texture and formation of shear bands in a hot rolled 7050 aluminum alloy. *Scripta Mater.*, 1998, **39**(4-5), 583-588.  
doi: 10.1016/s1359-6462(98)00200-0
18. Jena, P.K.; Mishra, B.; Siva Kumar, K. & Bhat, T.B. An experimental study on the ballistic impact behaviour of some metallic armour materials against 7.62 mm deformable projectile. *Mat. Des.*, 2010, **31**, 3308-16.  
doi:10.1016/j.matdes.2010.02.005
19. Yang, Y.; Zeng, Y.; Li, D.H. & Li, M. Damage and fracture mechanism of aluminium alloy thick-walled cylinder under external explosive loading. *Mat. Sci. & Eng. A*, 2008, **490**, 378-384.  
doi:10.1016/j.msea.2008.01.047
20. Srivathsa, B. & Ramakrishnan, N. A ballistic performance index for thick metallic armour. *Comp. Simulation Model Eng.*, 1998, **3**, 33-40.
21. Singh, B.B.; Sukumar, G.; Bhattacharjee, A.; Siva Kumar, K.; Bhat, T.B. & Gogia, A.K. Effect of heat treatment on ballistic impact behavior of Ti-6Al-4V against 7.62 mm deformable projectile. *Mat. & Des.*, 2012, **36**, 640-649.  
doi:10.1016/j.matdes.2011.11.030
22. Jena, P.K.; Savio, S.G.; Siva Kumar, K.; Madhu, V.; Mandal, R.K. & Singh, A.K. An experimental study on the deformation behavior of Aluminium armour plates impacted by two different non deformable projectiles. *Procedia Eng.*, 2017, **173**, 222-29.  
doi:10.1016/j.proeng.2016.12.001
23. ASM aerospace specification metals Inc.  
<https://asm.matweb.com/search/SpecificMaterial.asp?bassnum=ma7075t6> (Accessed on 29 Nov. 2022).

## CONTRIBUTORS

**Dr Pradipta Kumar Jena** obtained his PhD from Indian Institute of Technology, BHU, Varanasi and working as a Scientist in DRDO-DMRL, Hyderabad. His areas of interest include: Development of armour materials and kinetic energy penetrators also development of metallic armour materials like steel and aluminium armour, development of tungsten heavy alloys for kinetic energy penetrator applications. Contribution in the current study: He Carried out microstructural, texture, mechanical and ballistic testing.

**Dr Koppoju Suresh** obtained his PhD degree in Physics and is working as a Senior Scientist in International Advanced Research Centre for Powder Metallurgy and New Materials, Hyderabad. His research areas include: Investigation of microstructure using small angle x-ray/neutron scattering and transmission electron microscopy techniques, high energy and high performance rare earth permanent (NdFeB and SmCo) and ultra-soft magnets. Contribution in the current study: He Carried out small angle X-ray studies.

**Dr K. Sivakumar** obtained his PhD (Explosive compaction) from IIT, Bombay. He has retired as Scientist 'G' from DRDO-DMRL, Hyderabad. He has worked in the areas of development of armour materials and systems for various types of protective applications. Contribution in the current study: He contributed in ballistic testing analysis.

**Dr R.K. Mandal** obtained his PhD degree from Indian Institute of Technology BHU, Varanasi, India and working as a Professor at Indian Institute of Technology, BHU, Varanasi. His research area comprises materials engineering, synthesis and characterization of nanostructured materials, phase transformations, microstructural evolution. Contribution in the current study: He contributed in XRD and mechanical property analysis.

**Dr A.K. Singh** obtained his PhD degree from Banaras Hindu University, Varanasi, India. He has retired as Scientist 'G' from DRDO-DMRL, Hyderabad. His research area includes phase transformations of conventional titanium alloys and intermetallics, texture development in materials during deformation and recrystallization, structural characterization by Rietveld refinement technique and nanomaterials. Contribution in the current study: He contributed in texture analysis and correction of the paper.